Mitigating mechanical failure of crystalline silicon electrodes for lithium batteries by morphological design

Citation: An, Yonghao et al. "Mitigating Mechanical Failure of Crystalline Silicon Electrodes for Lithium Batteries by Morphological Design." Physical Chemistry Chemical Physics 17, 27 (June 2015): 17718–17728 © 2015 Royal Society of Chemistry (RSC)

As Published: http://dx.doi.org/10.1039/C5CP01385B

Publisher: Royal Society of Chemistry (RSC)

Persistent URL: http://hdl.handle.net/1721.1/111789

Version: Author's final manuscript: final author's manuscript post peer review, without publisher's formatting or copy editing

Mitigating the Mechanical Failure of Crystalline Silicon Electrodes for Lithium Batteries by Morphological Design

Article *in* Physical Chemistry Chemical Physics · June 2015

DOI: 10.1039/C5CP01385B

CITATIONS
5

READS
71

7 authors, including:

Brandon C Wood
Lawrence Livermore National Laboratory
68 PUBLICATIONS **589** CITATIONS
SEE PROFILE

Jianchao Ye
Lawrence Livermore National Laboratory
32 PUBLICATIONS **706** CITATIONS
SEE PROFILE

Ming Tang
Rice University
36 PUBLICATIONS **1,166** CITATIONS
SEE PROFILE

Hanqing Jiang
Arizona State University
137 PUBLICATIONS **6,007** CITATIONS
SEE PROFILE

Mitigating Mechanical Failure of Crystalline Silicon Electrodes for Lithium Batteries by Morphological Design

Yonghao An[a,b,c], Brandon C. Wood[b], Jianchao Ye[b], Yet-Ming Chiang[c], Y. Morris Wang[b], Ming Tang[*d], Hanqing Jiang[*a]

[a]School for Engineering of Matter, Transport and Energy, Arizona State University, Tempe, AZ 85286, USA

[b]Physical and Life Science Directorate, Lawrence Livermore National Laboratory, Livermore, CA 94550, USA

[c]Department of Materials Science and Engineering, Massachusetts Institute of Technology, MA 02139, USA

[d]Department of Materials Science and NanoEngineering, Rice University, Houston, TX 77024, USA

*Contact Emails: mingtang@rice.edu, Hanqing.Jiang@asu.edu

Although crystalline silicon (c-Si) anodes promise very high energy densities in Li-ion batteries, their practical use is complicated by amorphization, large volume expansion and severe plastic deformation upon lithium insertion. Recent experiments have revealed the existence of a sharp interface between crystalline Si (c-Si) and the amorphous Li_xSi alloy during lithiation, which propagates with a velocity that is orientation dependent; the resulting anisotropic swelling generates substantial strain concentrations that initiate cracks even in nanostructured Si. Here we describe a novel strategy to mitigate lithiation-induced fracture by using pristine c-Si structures with engineered anisometric morphologies that are deliberately designed to counteract the anisotropy in the crystalline/amorphous interface velocity. This produces a much more uniform volume expansion, significantly reducing strain concentration. Based on a new, validated

methodology that improves previous models of anisotropic swelling of c-Si, we propose optimal morphological designs for c-Si pillars and particles. The advantages of the new morphologies are clearly demonstrated by mesoscale simulations and verified by experiments on engineered c-Si micropillars. The results of this study illustrate that morphological design is effective in improving the fracture resistance of micron-sized Si electrodes, which will facilitate their practical application in next-generation Li-ion batteries. The model and design approach present in this paper also have general implications for the study and mitigation of mechanical failure of electrode materials that undergo large anisotropic volume change upon ion insertion and extraction.

1. Introduction

The increasing demand for the ever-spreading applications of lithium batteries in portable electronics, electrical/hybrid vehicles and smart grids calls for the development of electrode materials with significantly improved energy density, rate capability and life span[1-4]. Silicon as a Li-alloying anode has attracted enormous interest in recent years[5-9] due to its high theoretical specific capacity (3579 mAh/g for $Li15Si_4$, and 4200mAh/g for $Li_{22}Si_5$). Lithium insertion into crystalline silicon (c-Si) is observed to result in a transformation to an amorphous Li_xSi alloy (a-Li_xSi)[10], which is accompanied by large volume expansion of more than 300%.[6] Such a large volume change induces severe plastic deformation and causes the pulverization of silicon electrodes upon the first cycle of lithiation and rapid capacity fading[11]. Various approaches have been explored to prevent the Li-insertion-induced mechanical failure, including improving the supporting electrode components[12] and employing silicon nanostructures[6]. In particular, Si nanowires allow (de)lithiation-induced stress to be effectively relieved along the radial direction while maintaining fast electron transport in the axial direction, and their use has significantly

enhanced capacity retention and rate capability of Si anodes in recent years[6]. Nevertheless, Si nanowires[13, 14] and nanoparticles[15] can still form cracks during lithium insertion. For instance, Lee et al. found that more than 90% of <111> axially oriented c-Si nanopillars with diameters of 300-400 nm fractured upon first lithiation[13]. They concluded that nanopillars could only remain fracture-free below a critical size of 240–360 nm.

An important finding from recent experiments is that the volume change of c-Si nanostructures upon Li insertion is highly anisometric. Liu et al. observed that <112>-oriented silicon nanowires with circular cross sections evolve into a dumbbell shape after lithiation[14]. Lee et al. discovered that electrochemical lithium insertion causes round silicon nanopillars with <100>, <110> and <111> axial orientations to expand into anisometric shapes with 4-, 2- and 6-fold symmetries, respectively[16]. A common feature among all observations of nanowires is that swelling is most significant in the <110> direction and least along <111>, with <100> and <112> in between. Liu et al. performed in-situ high-resolution transmission electron microscopy (TEM) to characterize the electrochemical reaction at the growth front of a-Li_xSi in individual Si nanowires during lithium insertion[17]. Their experiment reveals the interface between a-Li_xSi and c-Si to be atomically sharp and migrate through a ledge mechanism involving lateral movement of steps on close-packed <111> planes. This migration process results in orientation-dependent interface mobility, which is shown by the modeling study of Yang et al[18] to be the origin of anisotropic swelling of c-Si nanowires. The anisometric shape change phenomenon has negative implications for the degradation of silicon anodes. Upon first lithiation, cracks form predominantly in the slow-swelling directions on the side surfaces of c-Si nanopillars[13], e.g. <100> for pillars with <110> axial orientation and <112> for <111> pillars. These cracks further grow upon subsequent electrochemical cycling, and contribute to impedance increases and loss

of electrical contact between the active material and current collector. They also expose more fresh silicon surfaces to the surrounding electrolyte, which leads to capacity fading due to the formation of solid-electrolyte interphase (SEI).

The concurrent processes of Li transport, phase transformation and elasto-plastic deformation in Si anodes have inspired numerous modeling works[19-25]. Several groups developed models to explain the anisometric volume expansion of *c*-Si nanowires upon lithiation[14, 18, 24]. Liu et al.[14] postulate an orientation dependent lithiation-induced strain in a-Li_xSi to explain the dumbbell shape of <112>-orientated nanowires. The study by Yang et al.[18, 24] relates the anisotropic swelling behavior to the orientation-dependent velocity of the a-Li_xSi/c-Si interface (ACI). In their work, an orientation-dependent and concentration-dependent Li diffusivity function, with a much smaller value in the interfacial region than in the amorphous phase, is introduced to numerically generate an anisotropic interface velocity. While simulations based on these models reproduce the morphological evolution of the nanopillars upon first lithiation, they can be improved in several aspects. First, the numerical approaches through which the orientation dependence of interface velocity is introduced in References 18 and 24 could be modified to more directly reflect the physical mechanism of c-Si/a-Li_xSi phase boundary motion, which is shown by experiment to be controlled by interface reaction kinetics[17] (as opposed to bulk diffusion kinetics). For interface-reaction controlled processes, the absorption or emission of atoms across interfaces is the rate-limiting step for phase boundary migration, yielding the following expression for the boundary velocity *v*:

$$v = M\Gamma \tag{1}$$

where Γ is the thermodynamic driving force for the interface reaction. *M* is the interface mobility or reaction rate constant, an intrinsic material property that could be assessed from experiment or atomistic calculation. The physical interpretation of Equation 1 is that the orientation dependence of *M* rather than the Li diffusivity results in the anisotropic interface velocity. Second, it is not straightforward to relate the anisotropy-controlling parameters in Reference [18] (notably, the interfacial diffusivity) to experimental measurement, which makes quantitative simulation challenging. Third, updating the interface location in these models requires solving the diffusion equation within the amorphous Li_xSi phase, which is computationally costly. For instance, in References 14, 18, and 24, and, a diffusivity 10^5 times that of the interface diffusivity is assigned to the bulk of a-Li_xSi to ensure that interface motion is not diffusion limited; such a large variation in diffusivity places a significant limit on the time step size in simulation. In addition, evaluation of the interface diffusivity value at the growth front of a-Li_xSi requires the determination of the orientation of the nearest interface segment, which is cumbersome.

In this paper we first describe a new simulation methodology to overcome the above mentioned limitations. Unlike previous models, the ACI location is evolved explicitly through Equation 1 using a front-tracking method. Interface mobility *M* hence becomes a natural model parameter, which can be determined experimentally or theoretically to improve the fidelity of simulation. Because the location of ACI is updated without the need to solve the diffusion equation in 3D space, the model is numerically very efficient and allows for simulations to be easily extended to 3D systems such as nanoparticles.

Using our interface-tracking model as a tool, we next explore the feasibility of improving the fracture resistance of Si anode by tailoring its morphology. Although nanoscaling Si electrode structures can significantly relieve the pulverization problem and enhance capacity

retention, it has the disadvantage of creating a large electrode/electrolyte interface area, which limits the packing density of active material and hence the overall energy density of the battery. Furthermore, side reactions at the electrode/electrolyte interfaces, including exothermic reactions under abuse conditions, are accelerated by the high surface-to-volume ratio and detrimental to battery safety. Here we show that rational design of Si electrode morphology provides an alternative strategy to mitigate crack initiation. The key underlying concept is to offset the anisotropic swelling of c-Si with a properly chosen anisometric geometry of the pristine anode, e.g. a non-circular cross section on a nanowire, which can promote more isometric volume expansion and lower tensile strain in the amorphous phase upon cycling to suppress electrode fracture. We note that morphological design has been employed to improve the functional properties (e.g. light absorption efficiency) of Si nanowires[26], but its application to improving mechanical properties has not previously been proposed or reported. Below we first present the details of our modeling method and validate its predictive capability by comparison with experimental results on circular Si nanowires and spherical Si nanoparticles documented in literature[13, 14, 27]. Next, we use our method to suggest specific morphologies for mitigating fracture, and demonstrate their effectiveness through simulations and experimental tests of shaped c-Si electrodes.

2. Model

In our model, the phase boundary between c-Si and a-Li_xSi is treated as an object of zero thickness. At the interface, c-Si is transformed into *a*-Li_xSi through the solid-state chemical reaction $xLi^+ + xe^- + Si \rightarrow Li_xSi$. The interface velocity is proportional to the reaction rate, and

according to Equation 1, the product of interface mobility M and the driving force of the reaction Γ, defined by

$$\Gamma = x(\mu'_{Li} - \mu^a_{Li}) + \mu^c_{Si} - \mu^a_{Si} - xF\phi \quad (2)$$

where $\mu^a_{Li/Si}$ are the chemical potentials of Li and Si in a-Li_xSi at the reaction front, μ'_{Li} and μ^c_{Si} are the chemical potential of Li in the counter-electrode and Si in c-Si, respectively, and ϕ is the electric potential relative to the counter-electrode. Notably, $\mu^a_{Li/Si}$ depend on not only the Li concentration but also the stress state of the amorphous phase. Sheldon et al.[28] report that stresses in Si electrodes make a modest but non-negligible impact on the equilibrium Li content at a given electric potential. A general expression for $\mu^a_{Li/Si}$ with stress contributions is[28]

$$\mu_i = \mu_i^{a\circ} + RT\ln(\gamma_i X_i) + V\sum_{j=1}^{3}\sigma_{jj}\left(\frac{\partial \epsilon_{jj}}{\partial N_i}\right)_{T,P,N_{j\neq i}} \quad (3)$$

where $\mu_i^{a\circ}$ (i=Li, Si) are the chemical potentials of Li/Si in their pure amorphous state, γ_i the activity coefficient, X_i the molar fraction, V the volume, σ_{jj} the stress and $(\partial\epsilon_{jj}/\partial N_i)_{T,P,N_{j\neq i}}$ the the variation in elastic strain due to changing the molar number N_i of Li or Si in the material. During the lithiation of c-Si electrodes, anisotropic swelling affects both stress development and Li diffusion within the amorphous shell, which could lead to non-uniform distribution of the Li concentration and stress along the reaction front. This consequently results in spatially varying reaction driving force according to Eq. 3. However, when phase transformation is interface-reaction limited, local equilibration is maintained within a-Li_xSi because Li diffusion is much faster than the reaction kinetics, leading to uniform chemical potentials of Li and Si through the amorphous phase. Therefore, it is reasonable to approximate Γ as a constant along ACI under

such circumstance. The orientation dependence of the interface velocity $v(\boldsymbol{n})$ is hence the same as that of the interface mobility $M(\mathbf{n})$. The critical feature size of a Si electrode below which this approximation is valid can be estimated as $a_c = D/v$, where D is Li diffusivity and v is interface velocity. Using representative values[17, 29, 30] $D = 1\times10^{-12} cm^2/s$ and v < 5 nm/min, we obtain a_c > 1 μm. A recent experimental study reports self-limiting lithiation behavior in Si nanowires, and the stress dependence of interface reaction rate or mobility is considered as a possible explanation[31]. However, there is no evidence so far to support that the stress effect on interface mobility is an important factor in the anisotropic swelling behavior of Si. M is thus considered as a function of orientation **n** only.

The functional form of $v(\boldsymbol{n})$ or $M(\boldsymbol{n})$ is constrained by the fact that they must conform to the crystallographic symmetry of c-Si, i.e., remain invariant under symmetry operations of c-Si. There exist various methods[32,33] to derive expressions that satisfy this symmetry requirement. Here we use the invariant theory[33, 34] to expand $v(\mathbf{n})$ as

$$v(\mathbf{n}) = A_1 I_1 + A_2 I_2 + A_3 I_3 + A_4 I_2^2 + \ldots \quad (4)$$

where $I_k(\mathbf{n})$ (k=1,2,3…) are polynomials of increasing degrees that are invariant with respect to cubic symmetry operations. The expressions for I_1, I_2 and I_3 and their values in several directions of interest are given in Table 1. The spherical plots of I_1, I_2 and I_3 are shown in Figure S1. We truncate the polynomial series at I_2^2 to make $v(\mathbf{n})$ tractable for simulations. Coefficients A_k (k=1-4) control the anisotropy of $v(\mathbf{n})$ and $M(\boldsymbol{n})$; their relative values can be evaluated from measurements or calculations of c-Si/a-Li_xSi interface velocities along different orientations. Though such data are still scarce, the in-situ TEM experiment by Liu et al.[17] provides two important observations, i.e., the interface velocity in <111> directions is vanishingly small and

{110} facets exhibit the highest growth rate. Based on these findings, we impose the following requirements on $v(\mathbf{n})$:

1) {111} interfaces have zero velocity: $v_{<111>} = 0$.
2) Interface velocity attains a global maximum in <110> directions: $v_{<110>} = v_{max}$.
3) The velocity of {100} is η times of that of {110}: $v_{<100>} = \eta\, v_{max}$, where η is an adjustable parameter with a value between 0 and 1.

We find that the above requirements are satisfied by the function

$$v(\mathbf{n}) = v_{max}\left(1 - 16(1-\eta)\left(I_2(\mathbf{n}) - \frac{1}{4}\right)^2 - 3(8+\eta)I_3(\mathbf{n})\right) \quad (5)$$

Equation 5 is used to evaluate the orientation interface velocity along all orientations in our simulations. We note that the accuracy of $v(\mathbf{n})$ can be improved by including higher order terms in Equation 4 with additional adjustable parameters fitted to interface velocity or mobility data once they become available.

Without a complete set of experimental or modeling data, the exact value of the anisotropy-controlling parameter η is difficult to ascertain. However, we found that the simulation results are rather insensitive to η, provided that the qualitative ordering of the interface velocities in <110>, <100>, and <111> remains unchanged (see Figure S3). The same ordering is employed in a previous modeling study[18]. A value of $\eta = 1/6$ is used throughout this paper. Though somewhat arbitrary, we justify this choice through model first-principles density functional theory (DFT) calculations, as detailed in the Supplementary Information. Other groups have previously used DFT calculations and the nudged elastic band method to extract Li reaction kinetics at Si surfaces. For instance, Cubuk et al. used a multiscale model based on DFT

and kinetic Monte Carlo to confirm that the {111} surface shows slower lithiation reaction kinetics than the {110} surface, but other facets were not explored[34]. Chan et al. considered the {100} surface in addition to {110} and {111}, but the relative ordering of the reaction barriers was found to depend nontrivially on Li surface concentration (and by extension, the surface flux), making comparison with observations of interface velocities difficult[35]. In the absence of a truly dynamical description of the reaction kinetics at each facet, we avoid such complexities by instead comparing the surface tension of (100), (111), and (110) facets, i.e. the dependence of surface energy on local Si tensile and compressive surface strain. Although not as sophisticated as the treatments in References [34, 35], our method provides a reasonable estimation of the relative differences in Li insertion barriers and hence reaction kinetics on various facets because surface tension reflects the ease (or difficulty) of the expansion or contraction of individual Si-Si bonds upon Li insertion. The calculations confirm that the (100) surface accommodates lattice strain much more poorly than (110), with (111) even poorer. Based on this input, we conclude that the interface velocities should order as $v_{<110>} >> v_{<100>} > v_{<111>}$, i.e. $\eta << 0.5$. The choice of η=1/6 is consistent with this finding. $v(\boldsymbol{n})$ at this η value is plotted as a function of interface orientation Figure S2(d).

In the numerical simulations of the lithiation process of c-Si nanopillars (2D) and nanoparticles (3D), the ACI position is updated at every time step according to Equation 5, using a front tracking method described in the Supporting Information. This method is found to be highly efficient and robust when the moving interface always has a convex shape, which is the case for the c-Si core. Because an interface-reaction limited process is assumed for the growth of a-Li_xSi, Li concentration is uniform in the amorphous shell and assigned a normalized value $\overline{c} \equiv c/c_{max} = 1$, where c_{max} is the maximal lithium concentration of the a-Li_xSi alloy. A uniform Li

concentration $\bar{c} = 0$ is assigned to the c-Si core because of the very small Li solubility in crystalline silicon. The Li concentration field in the anode is hence updated in the lithiation simulation without solving the diffusion equation. The maximal interface velocity v_{max} in Equation 5 is a function of the driving force Γ. Because the magnitude of v_{max} does not affect the morphological evolution and deformation of the electrode provided that the interface-reaction controlled growth condition is met, we use a normalized time in the simulation, defined as $\tau = tv_{max} / a$ where a is the electrode feature size (e.g. pillar or particle radius). The lithiation-induced volume expansion is assumed to be linear with Li concentration as $V = V_0(1+\beta\bar{c})$, where V_0 is the molar volume of c-Si and β=3.

Similar to previous works[18, 19, 24, 25, 36, 37], *c*-Si is modeled as a linear elastic material with Young's modulus $E_c = 130GPa$ and Poisson's ratio $\nu = 0.28$, under the assumption that the solubility of Li in c-Si is negligible. *a*-Li_xSi is treated as a perfect elastic-plastic material, the mechanical constitution of which is described by large deformation formulation. The elastic property of *a*-Li_xSi is assumed to be isotropic, given in the incremental form as

$$d\sigma_i = \frac{E_a}{1+\nu}\left(d\ln\lambda_i^e + \frac{\nu}{1-2\nu}\left(d\ln\lambda_1^e + d\ln\lambda_2^e + d\ln\lambda_3^e\right)\right) \tag{6}$$

where σ_i and λ_i^e (i=1…3) are the stress and elastic stretch in the principal directions, and elastic modulus $E_a = 12GPa$ and Poisson's ratio $\nu = 0.28$ are similar to values used in Refs.[37]. The Von Mises yielding criterion $\sigma_v = Y$ is applied to model plastic deformation, where the Von Mises stress σ_v is defined by

$$\sigma_v = \sqrt{\frac{1}{2}\left[\left(\sigma_1-\sigma_2\right)^2 + \left(\sigma_2-\sigma_3\right)^2 + \left(\sigma_3-\sigma_1\right)^2\right]} \tag{7}$$

The yield stress Y is set at a constant value of 0.5 GPa[38-40]. The incremental plastic strain in the principal directions is determined by the flow rule,

$$d\ln\lambda_i^P = \alpha(\sigma_i - \sigma_h) \tag{8}$$

where $\sigma_h = (\sigma_1 + \sigma_2 + \sigma_3)/3$ is the hydrostatic stress and α is a time-dependent scalar field satisfying

$$\alpha = \begin{cases} \alpha > 0, & \frac{d\sigma_V}{dt} > 0 \;\&\; \sigma_V = Y \\ 0, & others \end{cases} \tag{9}$$

α is determined by solving the mechanical boundary value problem. More detailed discussion about the elasto-plastic constitutive relation using large deformation theory can be found in our previous work.[22] We note that the plasticity model could be further elaborated to account for the viscosity effects and strain rate dependence in amorphous Li_xSi. More accurate evaluation of model parameters such as yield strength of a-Li_xSi from measurement will also improve the predicative power. Although the employment of different plasticity models and/or model parameters will affect the details of simulation results, it will not change qualitatively predictions on the anisotropic shape evolution of c-Si electrodes, which is mainly a consequence of geometric constraint imposed by anisotropic ACI movement. For instance, using the Cowper-Symonds overstress power law to approximate the perfectly plastic limit in Ref. 24, Yang et al. obtain similar results as in our model.

Simulation based on the above model is implemented in the commercial finite element package ABAQUS. More detailed implementation information is provided in the Supporting Information.

3. Results and Discussion

3.1 Lithiation of c-Si nanopillars with circular cross section shape

We first study the lithiation process of c-Si nanopillars with circular cross-sections. Si pillars of 100 nm radius with four different axial orientations, i.e. <100>, <110>, <111> and <112>, are simulated. For simplicity, a plane strain condition is applied in the axial direction of the pillars. The simulation result for <112> pillar is shown in Figure 1 as an example; results for other nanopillars are presented in Figure S4. The dumbbell shape of the lithiated <112> nanopillar obtained by our simulation shows good agreement with the TEM observations[14] (Figure 1(d)) and an earlier simulation by Yang et al.[18]. To shed more light on the shape evolution of the c-Si core, the normalized ACI velocity $r = v(\theta)/v_{\max}$ in the {112} plane is plotted in Figure 1(a). It displays a butterfly shape, which has a maximum in <110>, a second maximum at 55° away from <110> that approximately corresponds to <13 1 7>, and a minimum in <111>. As shown in Figure 1(b) and S4(d), the fastest moving {110} and {13 1 7} planes gradually become the dominant facets of the ACI when lithiation proceeds. The other orientations are eventually eliminated from the ACI, resulting in a faceted c-Si core. We refer to <110> and <13 1 7> as the primary ACI directions hereafter. As indicated by the maximal in-plane stress distribution in the cross section plane (Figure 1(c)), the crystalline core is always subjected to tensile stress upon lithiation due to Li-insertion-induced expansion of a-Li_xSi along the ACI (white line). In contrast, the stress state of the amorphous shell has two distinct regions — the stress is compressive in the region immediately behind the moving ACI (in dark blue), but flips to tensile values further away from ACI. Such a change of stress character in a-Li_xSi explains the surface-initiated fracture observed in experiments, and can be understood as follows. When a thin c-Si layer swept by the ACI transforms to a-Li_xSi, its volume expansion is constrained along the ACI by the adjacent untransformed c-Si core, which results in compressive hoop stress in the amorphous phase immediately behind the ACI. The amorphous layer deforms

plastically to accommodate the compressive stress. As the ACI moves further inward, the previously transformed a-Li_xSi layer now serves to constrain the volume expansion of the newly transformed a-Li_xSi layer from outside, which gives rise to tension in the outer shell.

The amorphous shell in the <112> pillar expands the most along the primary ACI directions, i.e. <110> and <13 1 7>, and shows minimal swelling along <111> because of the anisotropic interface velocity. a-Li_xSi in front of the <110> and <13 1 7> facets undergoes severe plastic deformation to satisfy geometry compatibility at the ACI. Concurrently, material is pulled away from <111> towards the primary ACI directions due to the volume conservation constraint of plastic deformation. As evident from Figure 1(b), such material flow accumulates increasingly large tensile strain near <111> orientations on the pillar surface and eventually amounts to a plastic necking instability that can initiate surface cracks in this direction.

The simulated morphological evolution sequences of <001>, <110> and <111> nanopillars upon lithiation are shown in Figure S4(a)-(c). They exhibit features similar to the lithiation process of the <112> pillar, including the formation of faceted *c*-Si cores, dominant swelling along the primary ACI directions and plastic necking along the slow lithiation orientation. The good agreement between the simulation results, experiments[16] and previous modeling studies[18, 22] establishes the validity of our modeling method.

3.2 Lithiation of an initially spherical c-Si nanoparticle

Next, we extend the simulation to the lithiation process of a spherical nanoparticle of radius a =100 nm. Figure 2(a) shows the orientation dependence of the ACI velocity in 3D space. $v(\mathbf{n})$ has a global maximum along <110>, a global minimum along <111> and a second local minimum along <100>. The shape evolution of the particle is shown in Figure 2(b). As lithiation

proceeds, the nanoparticle expands anisometrically, forming "hills" along <110> and "valleys" in the <100> and <111> directions. The colormap in Figure 2(b) represents the equivalent plastic strain (PEEQ) distribution on the particle surface. Interestingly, the maxima of PEEQ reside in the <110> orientations at early stages (e.g. $\tau = 0.1$) but change to <100> at late stages (e.g. $\tau = 1$). Figure 2(c) shows the evolution of the c-Si core shape. Similar to the 2D nanopillars, the fastest moving crystallographic planes {110} become increasingly dominant at the ACI as the c-Si core shrinks, eventually becoming a rhombic dodecahedron bounded by 12 {110} faces. The cross-section view of the particle perpendicular to the <111> direction amid lithiation shown in Figure 2(d) resembles remarkably the TEM image of a partially lithiated Si nanoparticle from Reference. [27]. To our knowledge, this is the first time that the observed Si particle morphology is quantitatively explained and it shows that the shape evolution of 3D Si electrode structures is also controlled by the ACI velocity anisotropy.

3.3 Morphological design of c-Si anode

The modeling studies by Yang et al.[18, 24] and by us establish a clear connection between the fracture of c-Si pillars and the strain concentration in the slow lithiation directions. In Figure 3, TEM images from the literature[13, 14] that display directional fractures in <100>- and <112>-oriented Si nanowires are compared against the PEEQ distributions in pillars with the same axial orientations at an intermediate lithiation time. The locations of cracks coincide with the highest tensile strain regions on the pillar surfaces, which are in the directions of lowest ACI velocity on the pillars (<110> for <100>-oriented pillar, <111> for <112>-oriented pillar). This correlation points out that fracture of c-Si anodes is initiated by the plastic necking instability induced anisotropic swelling. It also suggests that one way to suppress crack formation would be to reduce the degree of tensile strain concentration along the slowest-moving ACI directions. Here

we demonstrate that this goal can be achieved by engineering pillars with anisometric cross section shapes.

Our strategy is inspired by the finding that high tensile strain in the outer amorphous shell originates from anisometric volume expansion of a-Li_xSi that generates material flow from the slowest-moving to the primary ACI orientations. As the plastic flow continues with lithiation, the very limited amount of amorphous material present behind the ACI in the slow lithiation directions necessitates the development of a large tensile strain. However, if a pillar is given an anisometric cross-section shape with *larger dimensions along the slower moving directions*, the anisotropy in the ACI velocity could be offset by the directional dimensional difference to produce a more uniform volume expansion, thereby reducing material flow from slow to fast ACI orientations and easing strain concentration.

In exploring promising designs of anisometric cross section shapes, we notice from our simulations that upon lithiation, the c-Si core invariably evolves into a polygonal morphology (Figure 1 and S4), regardless of its initial shape. The polygons consist of facets corresponding to local ACI velocity maxima and vertices in the directions of local velocity minima. Such geometries satisfy our intuition-guided criterion for cross-section anisotropy. Moreover, the polygonal shapes remain stable as the c-Si core shrinks, which avoids drastic ACI morphology changes during lithiation that may lead to local stress/strain concentrations. Therefore, our proposed cross-sectional shape for c-Si pillars is a polygon that satisfies the following requirements:

i) *The polygon is bounded by sides perpendicular to the primary ACI directions that are the largest (and second largest if necessary) local maxima of interface velocity in the cross-sectional plane.*

ii) *The distance from each side to the center of the polygon is proportional to the velocity of that side.*

Requirement ii) ensures that the ACI maintains a *self-similar* shape throughout the lithiation process. For <100> and <111> pillars, the proposed cross sections are a simple square and regular hexagon with {110} facets, respectively (Figure S5). For {112} and {110} pillars, the cross sections consist of two groups of crystallographic planes, which correspond to the largest and second largest local maxima of the interface velocity (Figure 4 and S5).

We examine the effectiveness of the morphological designs through simulations. Using the <112> pillar as an example again, Figure 4(a) shows that its designed cross section is bounded by two {110} and four {13 1 7} sides. The distances from these sides to the center are set to a=100nm and l=0.91a, respectively. Comparison between Figure 4(b) and 1(b) clearly shows that the pillar with the designed cross section grows into a much more isometric morphology than the circular pillar upon Li insertion. The degree of isotropy of the pillar cross section can be quantitatively measured by the circularity parameter, defined as $C = 2\sqrt{\pi A} / L$, where A and L are the area and perimeter of the cross section, respectively. Figure 4(c) shows the circularity of <112> pillars with polygonal and circular cross sections as a function of lithiation time. C of the circular pillar starts at its maximal value of 1, but then continues to decrease with time and drops below 0.85 at the end of lithiation. In contrast, the polygonal pillar has a smaller circularity value of 0.95 at τ=0, but it rapidly increases with time and maintains a very high value above 0.97 until lithiation is complete.

The isometric volume expansion of the <112> polygonal pillar leads to significant reduction of strain concentration in the amorphous shell. The PEEQ distributions in the polygonal and circular pillars at various lithiation times are represented by color maps in Figure 4(b) and 1(b), respectively. The same color scales are used to facilitate comparison. It is evident that the magnitude of PEEQ in the amorphous shell—particularly on the pillar surface—is considerably lower in the polygonal pillar at any time. Figure 4(d) plots the angular distribution of PEEQ on pillar surface at τ=0.3 for both types of pillars. The strain peak in the <111> directions of the circular pillar is absent in the polygonal pillar. Instead, the maximal PEEQ occurs in the <110> directions, with a magnitude that is nevertheless much smaller than the tensile strain concentration seen for the circular pillar. The change in the orientation of PEEQ peak indicates that there is a plastic flow from <110> towards <111> in the amorphous shell of the polygonal pillar. Because <110> is the fastest-moving ACI orientation, there is always a sufficient amount of amorphous phase present behind the {110} facets such that the plastic flow does not trigger any necking instability, in contrast to the case of the circular pillar.

Simulations of <100>, <110> and <111>-type pillars with polygon cross sections are presented in Figure S5 and S6. Analogous to our observations for the <112> pillar, these pillars also exhibit significant improvement in the uniformity of volume expansion (e.g. circularity remains above 0.95 after an initial transient period), and substantial reduction of strain concentration in the amorphous shell compared to circular pillars. (The only exception is the <111>-oriented pillar, which has only a weak anisotropy of the ACI velocity in the cross section plane; as a result, even the circular pillar maintains a high level of isotropy during the lithiation process.) Our simulation results support the hypothesis that properly designed anisometric cross-sections of the c-Si pillar cross sections can counteract the anisotropic ACI velocity to achieve

much more isometric volume expansion and effectively mitigate the risk of Li-insertion-induced fracture.

A similar morphological design concept can also be applied to improve the fracture resistance of c-Si particles. The preferred particle geometry we propose is a rhombic dodecahedron with all twelve faces oriented normal to the <110> directions, as illustrated in Figure 5(a). Such morphology is identical to the converging shape of the shrinking c-Si core in a spherical particle (Figure 2(c)). After Li insertion starts, the polyhedral particle quickly obtains an approximately spherical shape with small "ridges" along the edges and shallow "dents" at the vertices of the polyhedron (Figure 5(a)). The degree of isotropy of the particle can be measured by the sphericity parameter, defined as $S = 2\left(6\pi^2 V\right)^{1/3} / A$, where V and A are the particle volume and surface area, respectively. Figure 5(b) compares the evolution of S for the spherical and polyhedral particles upon lithiation. After an initial stage, the polyhedral particle achieves and retains a superior sphericity value above 0.975. The more isometric swelling of the polyhedral particle produces a lower and more uniform distribution of PEEQ on the particle surface (Figure 5(a)) compared to the spherical particle (Figure 2(a)).

It is important to point out that because no characteristic length scale exists in the interface-reaction controlled lithiation process considerd in our model, the simulation results (morphological evolution and plastic strain distribution) are independent of the feature size of the electrodes. Therefore, our morphological design strategy can be applied to improve the fracture behavior not only of nanopillars or nanoparticles but also of c-Si structures of larger dimensions as long as bulk diffusion process is much faster than the interface reaction kinetics. Whereas synthesis of anisometric Si nanostructures may be accomplished through anisotropic crystal

growth[41] or etching[42-44], anisometric micron-sized Si structures such as micropillars can be more easily and precisely fabricated by conventional photolithography techniques. We recently prepared both p-type and n-type silicon micropillar arrays (diameter = 2 μm) with different cross section shapes on (100) Si wafers using plasma etching, and electrochemically lithiated them in lithium half cells[45] (details of the fabrication and electrochemical test methods can be found in the Supporting Information). It is found that the p-type micro-pillars exhibit higher fracture resistance than n-type micropillars, allowing us to compare the experimental morphologies of p-type pillars with large volume expansion against theoretical predictions. Figure 6 shows the morphology of <100> circular and square-shaped micropillars on p-type wafers (conductivity 445 mΩ) before and after partial lithiation that results in a volume expansion of ~200%. The initially square pillars have four <110> sides, matching our proposed geometry for the rationally designed polygonal cross section of <100>-oriented pillars (Figure S5(a)). Consistent with theoretical predictions shown in Figure 6(c) and (f), the cross sections of square pillars grow into a much more isometric morphology than the round pillars at the late stage of lithiation. The quantitative agreement between experiments and simulations confirms that our model can reliably predict the Li-insertion-induced shape evolution of micron-sized Si structures. On the other hand, we also systematically studied the effect of cross section geometry and atomic layer metallic coatings on the fracture behavior of n-type <100> micropillars during first lithiation[45]. It is discovered that by changing the cross section shape from circle to square with <110> sides, crack formation in <100> pillars is significantly delayed in the lithiation process. Related experimental results have been reported elsewhere[45], and they illustrate that morphological design is a powerful strategy to improve the fracture performance of c-Si anodes.

Our model is applicable to the initial lithiation process of c-Si electrodes. After first cycle, silicon anodes remain largely in the amorphous phase, and further Li insertion/extraction does not incur crystalline-to-amorphous phase transformations (or vice versa). However, the benefits of the proposed morphological design approach extends beyond the first electrochemical cycle. Si electrodes often exhibit the largest capacity drop[6] during the first discharge/charge because of various irreversible processes occurring to the electrode structure including cracking-induced loss of electrical contact. Mitigating fracture upon the first lithiation thus plays an important role in achieving high overall capacity retention. Furthermore,, because amorphous electrode materials usually have isotropic Li transport and mechanical properties, the isometric morphology obtained by the morphologically designed Si electrodes at the end of first cycle will promote a more uniform volume expansion and reduce strain/stress concentration in electrodes upon subsequent cycling. The low surface-to-volume ratios associated with the isometric electrode shapes also help enhance capacity retention by suppressing SEI formation.

Compared to nanostructured electrodes, microstructured electrodes have advantages in achieving higher packing density of active material, slower side reaction rates due to lower surface-to-volume ratios, and potentially lower cost. However, microscale Si anodes have seen very limited success in Li-ion batteries so far because of the severe pulverization they experience during charge/discharge. The morphological design approach we propose here could provide a promising way to mitigate this problem and enable the fabrication of fracture-resistant micron-sized Si electrodes.

The assumption employed in our model that the lithation of c-Si is interface-reaction limited is valid for electrodes with feature sizes on the order of a few micrometers, as estimated in Section 2. As the dimensions of c-Si electrodes further increase, Li diffusion in the amorphous

shell will play an increasingly important role in the phase transformation kinetics, which requires solving the diffusion equation in a-Li_xSi in conjunction with the mechanical governing equations and Eqs. 1 and 2 to determine ACI motion and electrode shape evolution. Because Li diffusion in the amorphous phase is isotropic, the ACI geometry and volume expansion of a-Li_xSi are expected to be more isometric in diffusion-controlled lithiation process in large Si electrodes. However, such electrodes become susceptible to pulverization despite the more isotropic swelling because internal fracture will become prevalent. The morphological design will thus be most effective for tailoring c-Si electrode structures in the size range of 1 – 10 μ m.

4. Conclusion

A continuum model is developed to simulate concurrent interface-reaction limited phase transformation, plastic deformation and morphological evolution in c-Si anodes upon lithiation. The model has advantages over previously proposed approaches in that i) it is more consistent with the experimentally observed interface reaction-limited lithiation mechanism, ii) the model parameters can be directly measured from experiments or calculated by atomistic simulations, and iii) it can be efficiently implemented to allow for numerical simulation of large scale and 3D systems. The agreement between simulated and experimental morphologies of lithiated Si nanopillars and nanoparticles confirms that anisotropy in the amorphous/crystalline interface mobility is ultimately responsible for the anisotropic swelling of Si anode, and fracture is initiated by plastic necking in regions of tensile strain concentration in the amorphous shell. Inspired by these findings, we propose specific design rules for generating polygon/polyhedron geometries of 2D or 3D c-Si anodes which stem the severe plastic flow between slow and fast lithiation directions that gives rise to strain concentration. Our simulations show that the suggested anisometric electrode shapes effectively counterbalance the orientation-dependent ACI

velocities, and that the electrodes undergo much more isometric expansion with substantially lower strain concentrations than those found in circular pillars or spherical particles. The predicted effects of morphological design on improving shape isotropy and fracture behavior of c-Si electrodes upon lithiation are directly corroborated by experimental comparison of (100) Si micropillars with conventional circular and optimally designed cross-sectional shapes. Our work establishes rationally motivated morphological design as a practical strategy for synthesizing fracture-resistant Si electrodes for Li-ion batteries. The modeling tool developed in this work is also useful for the study of other phase-changing electrode materials that undergo large volume change and plastic deformation upon charge/discharge.

Acknowledgements

Y.A. acknowledges financial assistance from the Lawrence Scholarship at LLNL. Y.A., Y.M.C. and M.T. are supported by DOE project number DE-SC0002626. The work of B.W., J.Y. and Y.M.W. was performed under the auspices of the US Department of Energy by LLNL under contract No. DE-AC52-07NA27344, and supported by the Laboratory Directed Research and Development (LDRD) programs of LLNL (12-ERD-053). H.J. acknowledges the support from NSF CMMI-1067947 and CMMI-1162619. The authors will like to thank Dr. R.J. Nikolic of LLNL to provide p-type silicon micropillars, and Dr. Tae Wook Heo of LLNL for useful discussions.

1. Tarascon, J. M.; Armand, M. *Nature* **2001,** 414, (6861), 359-367.
2. Arico, A. S.; Bruce, P.; Scrosati, B.; Tarascon, J. M.; Van Schalkwijk, W. *Nature Materials* **2005,** 4, (5), 366-377.
3. Armand, M.; Tarascon, J. M. *Nature* **2008,** 451, (7179), 652-657.
4. Goodenough, J. B.; Kim, Y. *Chemistry of Materials* **2010,** 22, (3), 587-603.
5. Wu, H.; Chan, G.; Choi, J. W.; Ryu, I.; Yao, Y.; McDowell, M. T.; Lee, S. W.; Jackson, A.; Yang, Y.; Hu, L. B.; Cui, Y. *Nat Nanotechnol* **2012,** 7, (5), 309-314.
6. Chan, C. K.; Peng, H. L.; Liu, G.; McIlwrath, K.; Zhang, X. F.; Huggins, R. A.; Cui, Y. *Nat Nanotechnol* **2008,** 3, (1), 31-35.

7. Magasinski, A.; Dixon, P.; Hertzberg, B.; Kvit, A.; Ayala, J.; Yushin, G. *Nature Materials* **2010,** 9, (4), 353-358.
8. Wang, B.; Li, X.; Luo, B.; Hao, L.; Zhou, M.; Zhang, X.; Fan, Z.; Zhi, L. *Advanced Materials* **2015**, 1526-1532.
9. Chen, Z.; Wang, C.; Lopez, J.; Lu, Z.; Cui, Y.; Bao, Z. *Advanced Energy Materials* **2015**, 5, 1401826.
10. Limthongkul, P.; Jang, Y. I.; Dudney, N. J.; Chiang, Y. M. *Acta Mater* **2003,** 51, (4), 1103-1113.
11. Kasavajjula, U.; Wang, C. S.; Appleby, A. J. *Journal of Power Sources* **2007,** 163, (2), 1003-1039.
12. Yu, C. J.; Li, X.; Ma, T.; Rong, J. P.; Zhang, R. J.; Shaffer, J.; An, Y. H.; Liu, Q.; Wei, B. Q.; Jiang, H. Q. *Advanced Energy Materials* **2012,** 2, (1), 68-73.
13. Lee, S. W.; McDowell, M. T.; Berla, L. A.; Nix, W. D.; Cui, Y. *P Natl Acad Sci USA* **2012,** 109, (11), 4080-4085.
14. Liu, X. H.; Zheng, H.; Zhong, L.; Huan, S.; Karki, K.; Zhang, L. Q.; Liu, Y.; Kushima, A.; Liang, W. T.; Wang, J. W.; Cho, J. H.; Epstein, E.; Dayeh, S. A.; Picraux, S. T.; Zhu, T.; Li, J.; Sullivan, J. P.; Cumings, J.; Wang, C. S.; Mao, S. X.; Ye, Z. Z.; Zhang, S. L.; Huang, J. Y. *Nano Letters* **2011,** 11, (8), 3312-3318.
15. Liu, X. H.; Zhong, L.; Huang, S.; Mao, S. X.; Zhu, T.; Huang, J. Y. *Acs Nano* **2012,** 6, (2), 1522-1531.
16. Lee, S. W.; McDowell, M. T.; Choi, J. W.; Cui, Y. *Nano Letters* **2011,** 11, (7), 3034-3039.
17. Liu, X. H.; Wang, J. W.; Huang, S.; Fan, F. F.; Huang, X.; Liu, Y.; Krylyuk, S.; Yoo, J.; Dayeh, S. A.; Davydov, A. V.; Mao, S. X.; Picraux, S. T.; Zhang, S. L.; Li, J.; Zhu, T.; Huang, J. Y. *Nat Nanotechnol* **2012,** 7, (11), 749-756.
18. Yang, H.; Huang, S.; Huang, X.; Fan, F. F.; Liang, W. T.; Liu, X. H.; Chen, L. Q.; Huang, J. Y.; Li, J.; Zhu, T.; Zhang, S. L. *Nano Letters* **2012,** 12, (4), 1953-1958.
19. Bower, A. F.; Guduru, P. R.; Sethuraman, V. A. *Journal of the Mechanics and Physics of Solids* **2011,** 59, (4), 804-828.
20. Zhao, K. J.; Pharr, M.; Vlassak, J. J.; Suo, Z. G. *J Appl Phys* **2011,** 109, (1).
21. Cui, Z. W.; Gao, F.; Qu, J. M. *Journal of the Mechanics and Physics of Solids* **2013,** 61, (2), 293-310.
22. An, Y.; Jiang, H. *Model Simul Mater Sc* **2013,** 21, (7), 074007.
23. Huang, S.; Fan, F.; Li, J.; Zhang, S.; Zhu, T. *Acta Mater* **2013,** 61, (12), 4354-4364.
24. Yang, H.; Fan, F.; Liang, W.; Guo, X.; Zhu, T.; Zhang, S. *Journal of the Mechanics and Physics of Solids* **2014,** 70, (0), 349-361.
25. Chen, L.; Fan, F.; Hong, L.; Chen, J.; Ji, Y. Z.; Zhang, S. L.; Zhu, T.; Chen, L. Q. *Journal of the Electrochemical Society* **2014,** 161, (11), F3164-F3172.
26. Kim, S.-K.; Day, R. W.; Cahoon, J. F.; Kempa, T. J.; Song, K.-D.; Park, H.-G.; Lieber, C. M. *Nano Letters* **2012,** 12, (9), 4971-4976.
27. McDowell, M. T.; Ryu, I.; Lee, S. W.; Wang, C. M.; Nix, W. D.; Cui, Y. *Advanced Materials* **2012,** 24, (45), 6034-+.
28. Sheldon, B. W.; Soni, S. K.; Xiao, X.; Qi, Y. *Electrochemical and Solid-State Letters* **2011,** 15, (1), A9-A11.
29. Tritsaris, G. A.; Zhao, K. J.; Okeke, O. U.; Kaxiras, E. *Journal of Physical Chemistry C* **2012,** 116, (42), 22212-22216.
30. Ding, N.; Xu, J.; Yao, Y. X.; Wegner, G.; Fang, X.; Chen, C. H.; Lieberwirth, I. *Solid State Ionics* **2009,** 180, (2-3), 222-225.
31. Liu, X. H.; Fan, F. F.; Yang, H.; Zhang, S. L.; Huang, J. Y.; Zhu, T. *Acs Nano* **2013,** 7, (2), 1495-1503.
32. Haxhimali, T.; Karma, A.; Gonzales, F.; Rappaz, M. *Nature Materials* **2006,** 5, (8), 660-664.
33. Qin, R. S.; Bhadeshia, H. K. D. H. *Acta Mater* **2009,** 57, (7), 2210-2216.

34. Cubuk, E. D.; Wang, W. L.; Zhao, K. J.; Vlassak, J. J.; Suo, Z. G.; Kaxiras, E. *Nano Letters* **2013,** 13, (5), 2011-2015.
35. Chan, M. K. Y.; Wolverton, C.; Greeley, J. P. *Journal of the American Chemical Society* **2012,** 134, (35), 14362-14374.
36. Zhao, K. J.; Pharr, M.; Cai, S. Q.; Vlassak, J. J.; Suo, Z. G. *Journal of the American Ceramic Society* **2011,** 94, S226-S235.
37. Hopcroft, M. A.; Nix, W. D.; Kenny, T. W. *J Microelectromech S* **2010,** 19, (2), 229-238.
38. Hertzberg, B.; Benson, J.; Yushin, G. *Electrochemistry Communications* **2011,** 13, (8), 818-821.
39. Kushima, A.; Huang, J. Y.; Li, J. *Acs Nano* **2012,** 6, (11), 9425-9432.
40. Chon, M. J.; Sethuraman, V. A.; McCormick, A.; Srinivasan, V.; Guduru, P. R. *Physical Review Letters* **2011,** 107, (4), 045503.
41. Kim, S. K.; Day, R. W.; Cahoon, J. F.; Kempa, T. J.; Song, K. D.; Park, H. G.; Lieber, C. M. *Nano Letters* **2012,** 12, (9), 4971-4976.
42. Seidel, H.; Csepregi, L.; Heuberger, A.; Baumgartel, H. *Journal of the Electrochemical Society* **1990,** 137, (11), 3626-3632.
43. Seidel, H.; Csepregi, L.; Heuberger, A.; Baumgartel, H. *Journal of the Electrochemical Society* **1990,** 137, (11), 3612-3626.
44. Huang, Z.; Geyer, N.; Werner, P.; de Boor, J.; Goesele, U. *Advanced Materials* **2011,** 23, (2), 285-308.
45. Ye, J. C.; An, Y. H.; Heo, T. W.; Biener, M. M.; Nikolic, R. J.; Tang, M.; Jiang, H.; Wang, Y. M. *Journal of Power Sources* **2014,** 248, (0), 447-456.

Table 1. Expressions of invariant polynomials $I_1(\mathbf{n})$, $I_2(\mathbf{n})$ and $I_3(\mathbf{n})$ and their values for several representative directions.

$< hkl >$	$<100>$	$<110>$	$<111>$	$<112>$
(n_1, n_2, n_3)	$(1,0,0)$	$\left(\frac{1}{\sqrt{2}}, \frac{1}{\sqrt{2}}, 0\right)$	$\left(\frac{1}{\sqrt{3}}, \frac{1}{\sqrt{3}}, \frac{1}{\sqrt{3}}\right)$	$\left(\frac{1}{\sqrt{6}}, \frac{1}{\sqrt{6}}, \frac{2}{\sqrt{6}}\right)$
$I_1 = n_1^2 + n_2^2 + n_3^2$	1	1	1	1
$I_2 = n_1^2 n_2^2 + n_2^2 n_3^2 + n_3^2 n_1^2$	0	1/4	1/3	1/4
$I_3 = n_1^2 n_2^2 n_3^2$	0	0	1/27	1/54

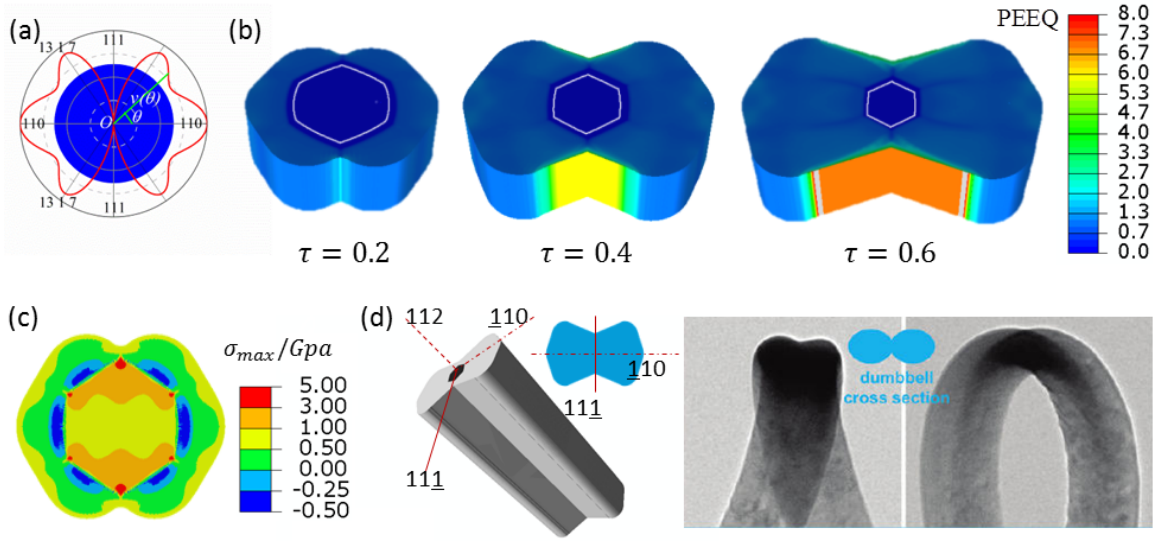

Figure 1. Lithiation simulation of a <112> c-Si nanopillar with an initially circular cross section. (a) Orientation dependence of the ACI velocity v in the (112) plane. (b) Snapshots of nanopillar morphology, ACI (white solid line), and equivalent plastic strain (PEEQ) represented by color maps at normalized lithiation times τ = 0.2, 0.4, 0.6. (c) Distribution of maximum in-plane stress on the pillar cross-sectional plane at τ = 0.2. (d) Comparison of the simulated dumbbell morphology of the lithiated <112> pillar (left) with the TEM image of a <112> nanowire (right) (reprinted with permission from Reference [14]. Copyright (2011) American Chemical Society).

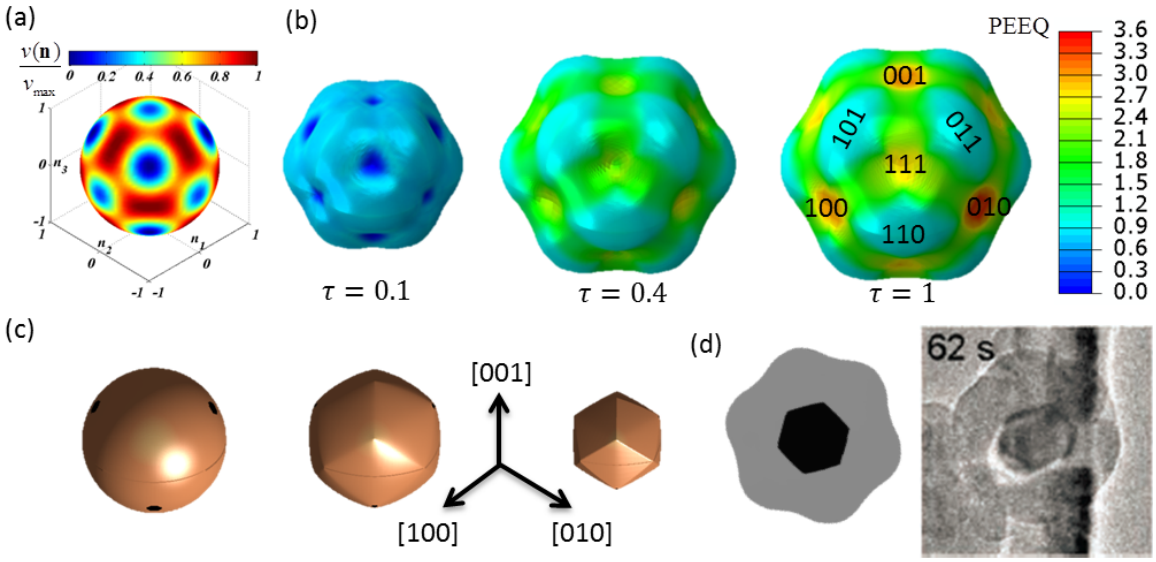

Figure 2. Lithiation simulation of a c-Si spherical nanoparticle. (a) Orientation dependence of the ACI velocity $v(\mathbf{n})$ in 3D space. (b) Snapshots of particle morphology and PEEQ distribution on the particle surface represented by color maps at τ = 0.1, 0.4, 0.6. (c) Snapshots of c-Si core morphology at τ = 0, 0.1, 0.4. (d) Comparison of the simulated morphology of the amorphous shell and crystal core at time τ = 0.4 viewed in the <111> direction (left) with the analogous TEM image (right) of a partially lithiated c-Si nanoparticle (reprinted with permission from Refrence [27]. Copyright (2011) Wiley).

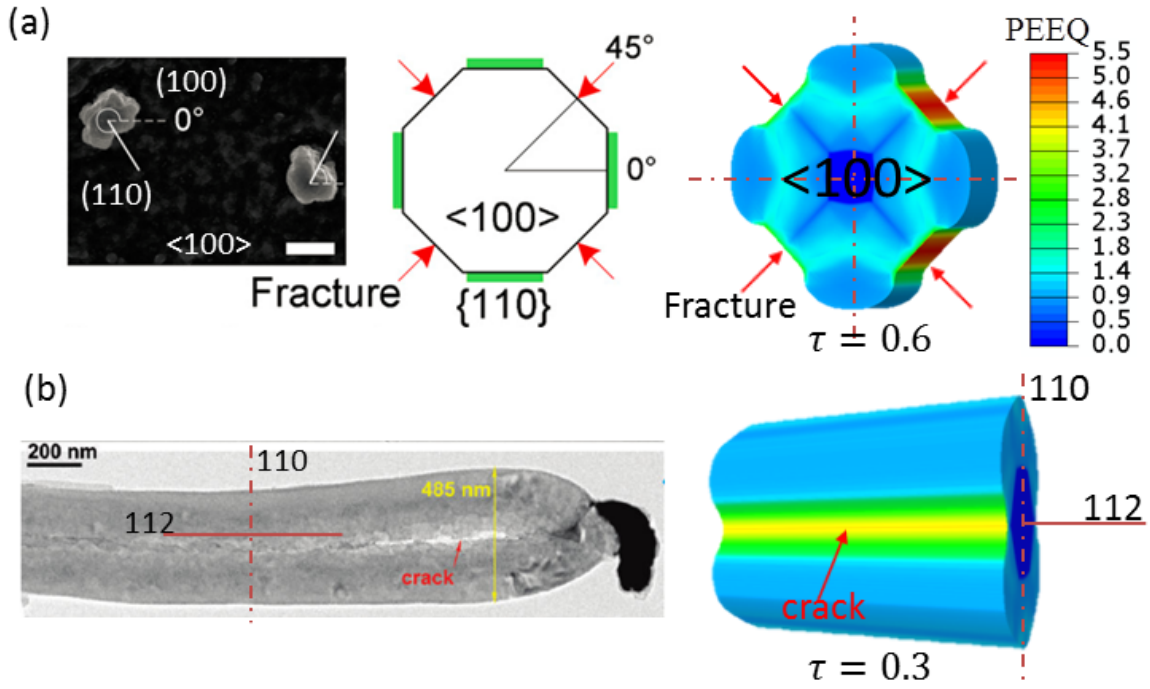

Figure 3. Comparison of the directions of fracture observed in experiments (left) and of maximum plastic strain concentration in our simulations (right) for (a) <100> and (b) <112> nanowires suggests that cracks initiate on surface regions of highly concentrated strain upon lithiation. Microscopic image of <100> nanopillars is reprinted from Reference[13], and microscopic image of <112> nanowire is reprinted with permission from Reference [14] (Copyright (2011) American Chemical Society).

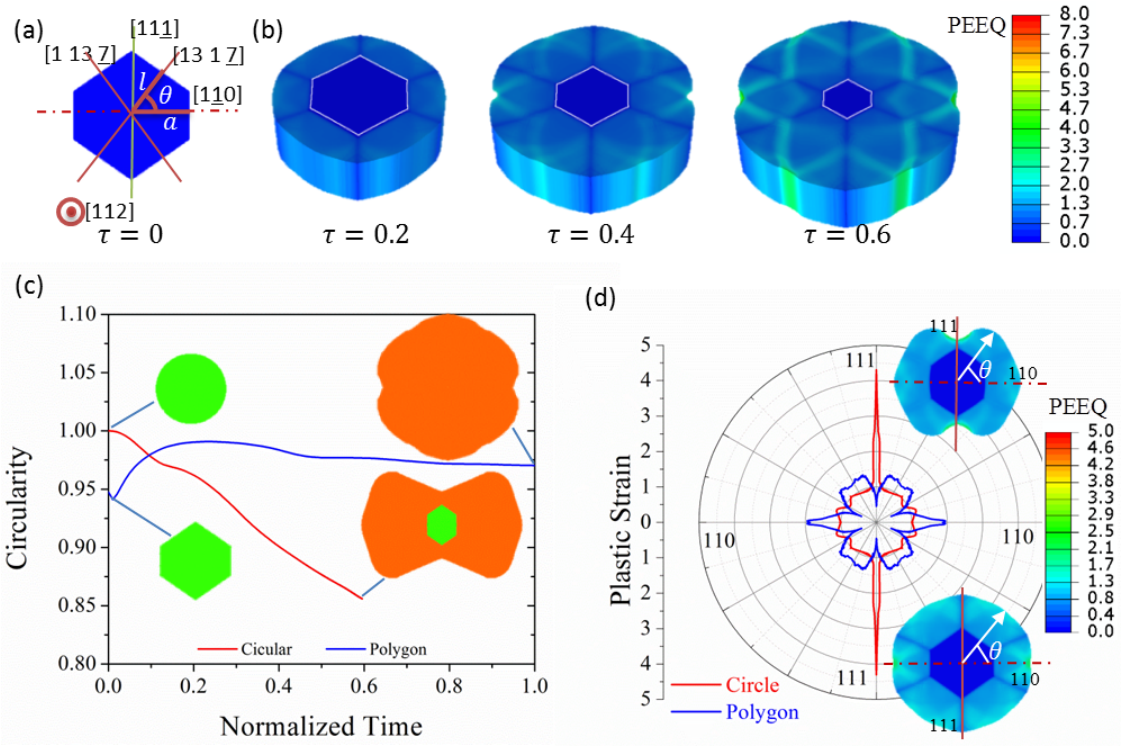

Figure 4. Lithiation simulation of a <112> nanopillar with a polygon cross section designed according to our proposed rules. (a) Original morphology of the pillar cross section with θ=55° and l/a =0.91. (b) Snapshots of nanopillar morphology, ACI (white solid line) and PEEQ distribution represented by color maps at τ = 0.2, 0.4, 0.6. (c) Time dependence of the circularity of initially polygonal and circular pillars upon lithiation. (d) Angular distribution of PEEQ on the surface of polygonal and circular pillars at time τ = 0.3.

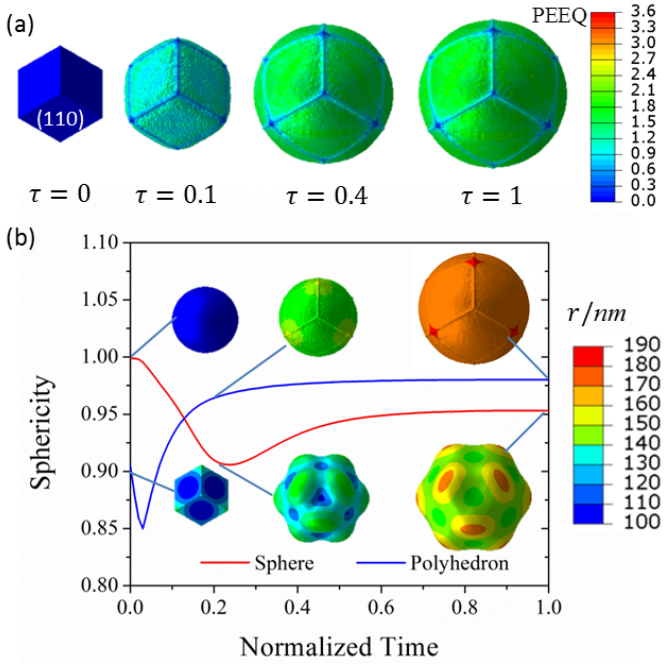

Figure 5. Lithiation simulation of a c-Si particle with rhombic dodecahedron geometry designed according to our proposed rules. (a) Snapshots of particle morphology and PEEQ distribution on the particle surface represented by color maps at τ = 0, 0.1, 0.4, 0.6. (b) The sphericity of initially polyhedral and spherical particles as a function of lithiation time. Colors in the insets indicate the distance of the particle surface to its center.

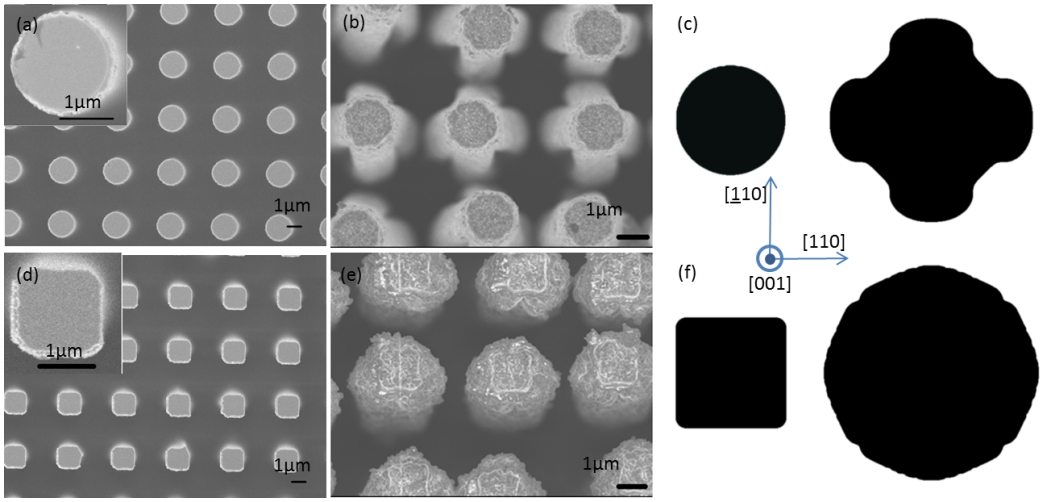

Figure 6. Comparison between SEM images and simulation results of the morphology change upon lithiation of <100> micropillars with different cross-section geometries. (a) and (d) are pristine pillars with circular cross sections and with square cross sections consisting of {110} edges, respectively. (b) and (e) are the same respective geometries after partial lithiation with volume expansion of c.a. 200%. (c) and (f) show the corresponding simulated morphologies of initially circular and square pillars at normalized lithiation times $\tau = 0$ (left) and $\tau = 0.4$ (right, with comparable volume expansion as in (b) and (e)), demonstrating very good agreement with the SEM images.

Supporting Information

Mitigating Mechanical Failure of Crystalline Silicon Electrodes for Lithium Batteries by Morphological Design

Yonghao An[a,b,c], Brandon C. Wood[b], Jianchao Ye[b], Yet-Ming Chiang[c], Yinmin Morris Wang[b], Ming Tang[*d], Hanqing Jiang[*a]

[a]School for Engineering of Matter, Transport and Energy, Arizona State University, Tempe, AZ 85286, USA

[b]Physical and Life Science Directorate, Lawrence Livermore National Laboratory, Livermore, CA 94550, USA

[c]Department of Materials Science and Engineering, Massachusetts Institute of Technology, MA 02139, USA

[d]Department of Materials Science and NanoEngineering, Rice University, Houston, TX 77024, USA

*Contact Emails: mingtang@rice.edu, Hanqing.Jiang@asu.edu

Additional Details of Simulation Method

In numerical simulations of the lithiation process, the loci of ACI are updated by a front tracking method. As illustrated in Figure S1, the ACI, which is a curve for 2D pillar simulations and surface for 3D particle simulations, is discretized by a set of points with equal separation. A sufficient number of points, typically 360 points for 2D and 64800 points for 3D simulations, are used to ensure the convergence of simulations. The tangential lines or planes at these points are determined. For each time step Δt, the tangent lines or planes are moved inwards along their normals by a distance $v(\boldsymbol{n})\Delta t$, where $v(\boldsymbol{n})$ is the orientation-dependent interface velocity evaluated by Equation 4 in the main text, and the new positions of ACI are determined by the

envelope of the updated tangent lines or planes. Following the update of ACI positions, the Li concentration field is also updated by assigning $\overline{c}$ =0 inside ACI and $\overline{c}$ =1 outside ACI. In addition, a smooth variation of $\overline{c}$ between 0 and 1 is imposed within a very thin layer across ACI to facilitate numerical convergence. The algorithm described above is implemented in ABAQUS user subroutine UTEMP. Another user subroutine UEXPAN is employed to specify the stress-free strain of *a*-Li_xSi resulting from lithiation-induced volume expansion in a way consistent with the total Lagrangian description for large deformation (see detailed discussion is our previous work[1]). The mechanical constitution is implemented by ABAQUS build-in modules for concentration-dependent properties, using the implicit plastic-elastic solver with the nonlinear geometry option turned on for large deformation problems.

Additional Details of Experimental Method

Micropillars on (100) Si wafers were defined photolithographically with masks in circle and square shapes. The latter has edge orientations along {110} planes. The diameter, spacing, and height of the micropillars are 2 μm, 2 μm, and 50 μm, respectively. The micropillars were etched out by a Bosch process[2] during which the isotropic etching step using 25 sccm SF_6 plasma and the passivizing polymerization step using 80 sccm C_4F_8 were alternated repeatedly until the desired height was achieved.

Swagelok-type half-cells were assembled in Argon-filled glove box with oxygen and water content less than 1 ppm for electrochemical lithiation. 1M LiPF6 in mixed ethylene carbonate (EC)/ diethyl carbonate (DEC)/ dimethyl carbonate (DMC) (1:1:1 in volume) was used as the electrolyte. Two layers of polypropylene microporous films (Celgard 3501) were used as

the separator. Si micropillars on wafer chip were directly assembled into the cell as the working electrode and lithium chip with thickness of 250 μm and diameter of 9 mm was adopted as the counter electrode. Partial lithiation was carried out in a Maccor 4304 battery cycler. The circular p-type micropillars shown in Figure 6(a) was lithiated at constant current density of 11 mA/cm^2 for 2000 s. The square p-type micropillars shown in Figure 6(d) was lithiated by scanning the cell voltage from the open circuit potential (~3V vs Li/Li$^+$) to 50 mV at a constant scan rate of 0.1 mV/s and then held at 50 mV for 20 hours. Afterwards the micropillar samples were washed with DMC, dried in a glove box and sealed in Ar-filled glass vials to be taken out for scanning electron microscopy (SEM) characterizations. SEM analysis was performed on a JOEL 7401-F system with an accelerating voltage of 2 kV and a working distance of ~6 mm.

Evaluation of the Anisotropy Parameter η

In the main text, the parameter η is used to describe the relative lithiation velocity along <100> with respect to <110>. A η value of 1/6 is used in simulation and the ordering of interface velocities in three main directions is set as: $v_{<111>} < v_{<100>} < v_{<110>}$. As a motivation for our choice of η and this ordering, we performed density functional theory (DFT) calculations of strain energy for thin surface slabs aligned along each of these directions. Each of the slabs was eight layers thick and carved from the corresponding bulk geometry. Surface reconstruction and atomic relaxation are not considered in the calculations, since there is no evidence that reconstruction will occur at the reaction front with lithiated *a*-Si, where ion mobility and entropy are high, and ions are freely available to passivate dangling bonds and equilibrate local potentials. The system therefore simulates two surface-vacuum interfaces with four independent layers each; the thin slabs were deliberately chosen so as to ensure that the calculated strain energies are

associated with surface rather than bulk character. To compute the strain energies, biaxial strain was applied within the surface plane only.

Periodic boundary conditions were applied, with 12 Å vacuum inserted perpendicular to the slab direction. An ultrasoft pseudopotential[3] with the Perdew-Burke-Ernzerhof (PBE) exchange-correlation functional[4] was employed for Si, with plane wave and charge density cutoffs of 24 Ry and 240 Ry, respectively, as implemented in the Quantum ESPRESSO code[5]. A Monkhorst-Pack[6] **k**-point mesh was used, based on a primitive-cell sampling of (6×6×6) and scaled appropriate to the surface of interest.

The Li insertion barrier is expected to correlate with the strain energy associated with locally expanding the slab parallel to the surface, so as to accommodate the diffusing Li. However, because the surface boundary conditions are fixed by the underlying crystalline Si lattice immediately beyond the amorphous-crystalline interface, we assume that local expansion must be accompanied by secondary local lattice compression, such that the total area of the surface is conserved. Accordingly, we examine the surface slabs under both tensile and compressive strain.

The area-specific strain energy for the slabs is shown as a function of strain in Figure S7(a). Note that the strain is defined relative to the equilibrium bulk lattice parameter, which does not necessarily correspond to the equilibrium lattice parameter of the surface slab due to intrinsic surface stress. Accordingly, the (100) and (111) surfaces have intrinsic compressive surface stress (minimum strain energy occurs below the bulk equilibrium lattice spacing), whereas the (110) surface has weak intrinsic tensile surface stress. To estimate the total strain energy *s* introduced by straining the lattice to accommodate Li insertion, we average the area-

normalized strain energy induced by tension with the equivalent quantity induced by compression, according to:

$$s = \frac{\Delta E^{+} + \Delta E^{-}}{2A_0}$$

where ΔE^{+} and ΔE^{-} are changes in total internal energy associated with the application of local tensile (+) and compressive (-) strain, and A_0 is the surface area of the slab at the equilibrium bulk lattice parameter. Note that this definition assumes the total surface area of the slab is conserved, as indicated above. As shown in Figure S7(b), the quantity s is smallest for the (110) plane and largest for the (111) plane, with the intermediate (100) result far closer to the (111) value than the (110) value. This means that the relative interface velocities of reaction fronts perpendicular to these planes, which are exponentially dependent on the insertion barriers via an Arrhenius relation, should have the ordering $v_{<110>} >> v_{<100>} > v_{<111>}$. We can use our computed values of s to calculate a composite strain ratio $r = \frac{s_{(111)} - s_{(100)}}{s_{(111)} - s_{(110)}}$, which describes the relative insertion barrier along <100> with respect to <110> and <111> and is related to the choice of the parameter η. For non-negligible strains, the ratio r has an upper bound of ~0.4, but decreases with increasing magnitude of the local surface strain induced upon Li insertion. In the immediate vicinity of Li, it is reasonable to assume that local areal strains greater than 10% may be observed, which lowers the expected value of r to less than 0.2. Considering the exponential dependence of reaction front velocity on reaction energy barrier, we conclude that η must be a small value significant lower than 0.5, which justifies our choice of 1/6. Notably, as we show for one example geometry in Figure S7, our conclusions do not change qualitatively if we set η to be even smaller (i.e., zero).

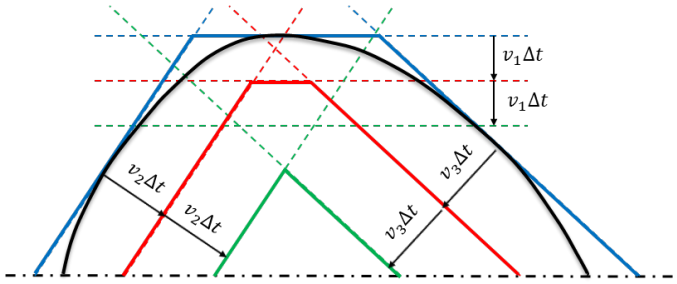

Figure S1. Illustration of how the front tracking method updates ACI positions. Initially, the ACI (black line) is discretized by a set of points with equal separation and their tangent lines form an envelope (blue lines) of ACI. Upon every time step, the tangential lines move inwards by a distance of $v(\mathbf{n})\Delta t$ in their normal directions, and the envelope they form (red and green lines) determines the new positions of ACI.

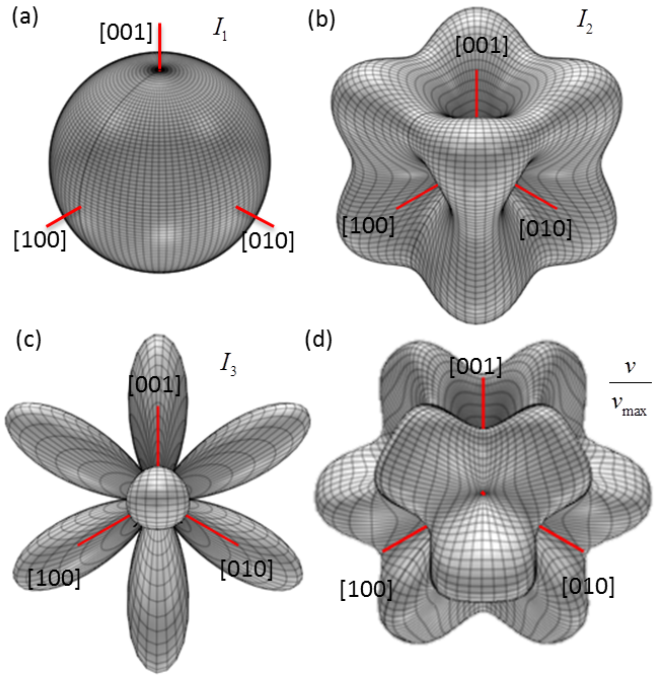

Figure S2. Plots of invariant polynomials (a) $I_1(\mathbf{n})$, (b) $I_2(\mathbf{n})$ and (c) $I_3(\mathbf{n})$ in spherical coordinate. (d) Spherical plot of normalized ACI velocity, $v(\mathbf{n})/v_{max}$, for parameter η=1/6.

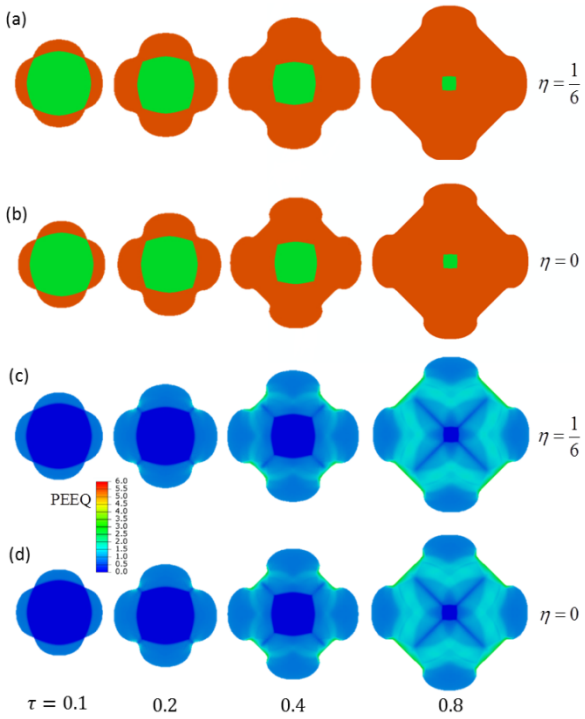

Figure S3. Effect of the value of anisotropy parameter η on simulation results of the lithiation of c-Si pillars. Snapshots of pillar morphology and PEEQ distribution in a <100> pillar at different normalized lithiation times are shown in (a) and (c), respectively for η = 1/6, and (b) and (d) for η = 0. Results for the two values are very similar, confirming the insensitivity of our results to the specific value of η.

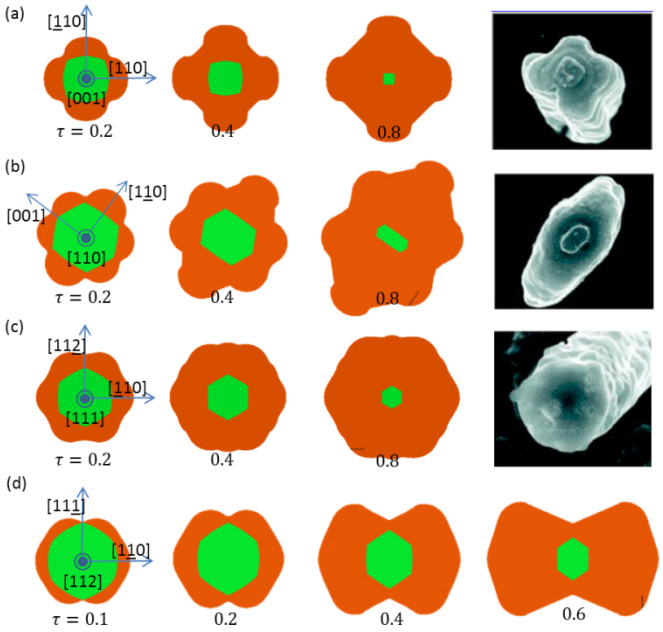

Figure S4. Lithiation simulation of c-Si pillars of four typical axial orientations. Snapshots of the morphology of a-Li_xSi shell (red) and c-Si core (green) at different lithiation times are shown for (a) <100>, (b) <110>, (c) <111> and (d) <112> pillars. SEM images of Si nanopillar morphology from Reference7 are also shown in (a)-(c) for comparison with simulation.

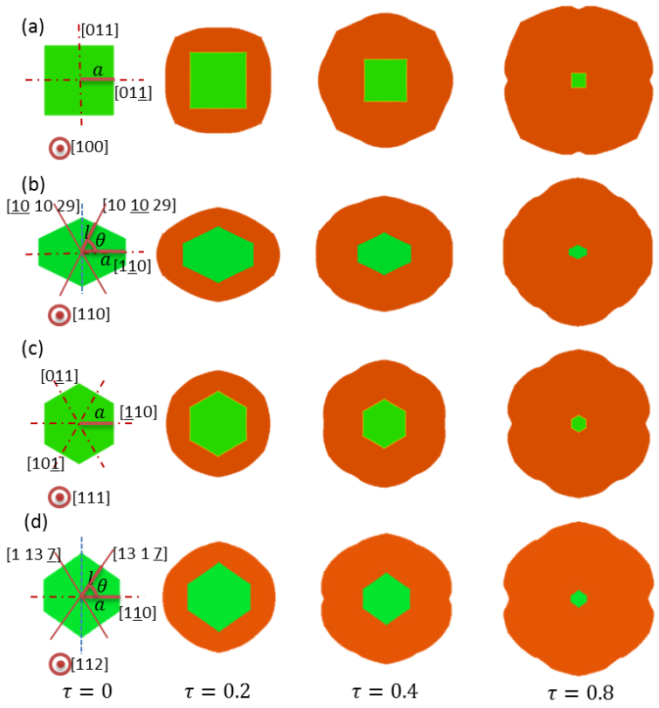

Figure S5. Lithiation simulation of c-Si pillars with designed polygonal cross section shapes. The original cross sections at τ=0 and snapshots of the morphology of a-Li_xSi shell (red) and c-Si core (green) at τ = 0.2, 0.4 and 0.8 are shown for (a) <100>, (b) <110>, (c) <111> and (d) <112> pillars.

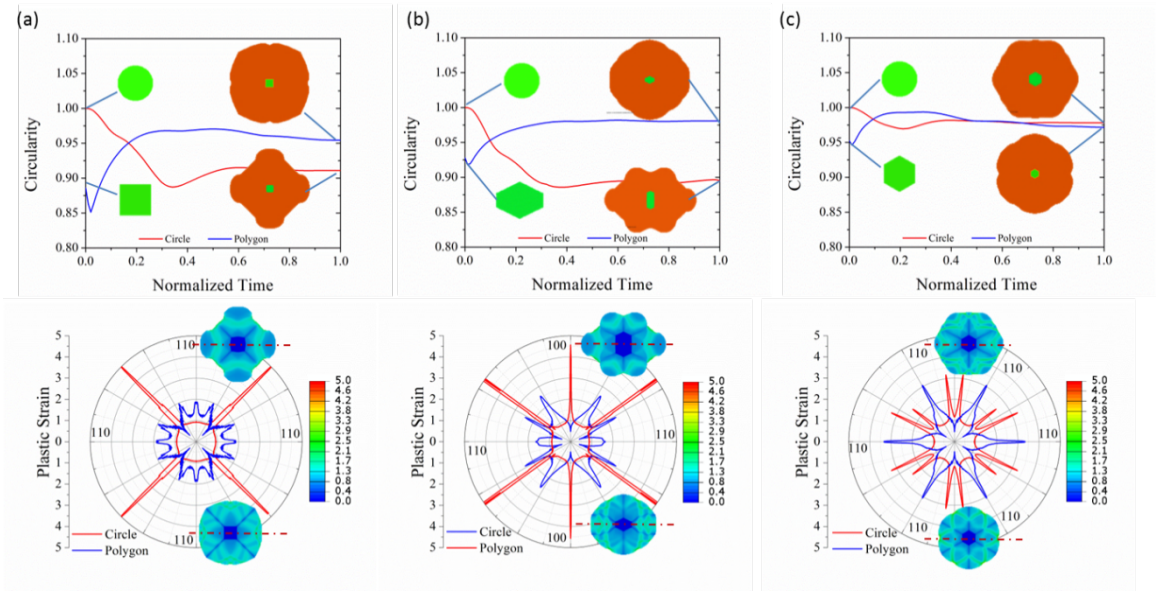

Figure S6. Comparison of the time evolution of the circularity (upper panel) and PEEQ distribution (at $\tau = 0.6$) within the cross section plane (lower panel) of circular (red curves) and polygonal pillars (blue curves) for (a) <100>, (b) <110> and (c) <111>-oriented pillars.

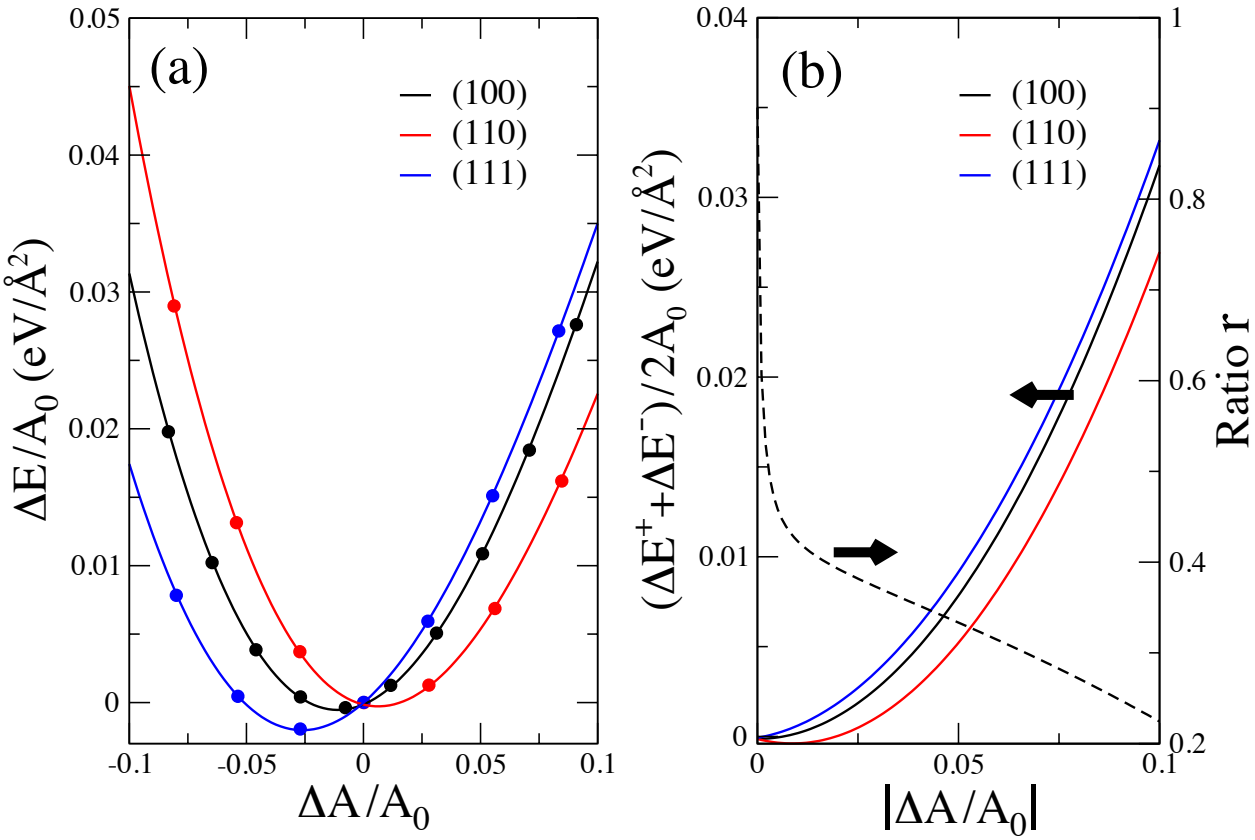

Figure S7. Procedure for estimating ordering of Li reaction front velocities based on strain induced in a Si surface slab upon lithiation, calculated by DFT. (a) Area-normalized strain energy $\Delta E / A_0$ for the (100), (110), and (111) surface slabs. Here, $\Delta A / A_0$ is the relative areal strain (negative/positive = compressive/tensile; the zero value represents the surface area at the equilibrium bulk lattice parameter), and ΔE is the associated change in total internal energy. (b) Left axis: Total area-normalized strain energy $s = \left(\Delta E^{+} + \Delta E^{-}\right) / 2A_0$ as a function of local strain magnitude $|\Delta A / A_0|$, obtained by averaging the surface slab strain energy under local compressive strain and under tensile strain. Here, ΔE^{+} and ΔE^{-} are changes in total internal energy associated with the application of tensile (+) and compressive (-) strain of the same magnitude. Right axis: Dependence of the ratio r on $|\Delta A / A_0|$.

References

1. An, Y.; Jiang, H. *Model Simul Mater Sc* **2013,** 21, (7), 074007.
2. Shao, Q.; Voss, L. F.; Conway, A. M.; Nikolic, R. J.; Dar, M. A.; Cheung, C. L. *Applied Physics Letters* **2013,** 102, (6), -.
3. Vanderbilt, D. *Phys Rev B* **1990,** 41, (11), 7892-7895.
4. Perdew, J. P.; Burke, K.; Ernzerhof, M. *Physical Review Letters* **1996,** 77, (18), 3865-3868.
5. Paolo, G.; Stefano, B.; Nicola, B.; Matteo, C.; Roberto, C.; Carlo, C.; Davide, C.; Guido, L. C.; Matteo, C.; Ismaila, D.; Andrea Dal, C.; Stefano de, G.; Stefano, F.; Guido, F.; Ralph, G.; Uwe, G.; Christos, G.; Anton, K.; Michele, L.; Layla, M.-S.; Nicola, M.; Francesco, M.; Riccardo, M.; Stefano, P.; Alfredo, P.; Lorenzo, P.; Carlo, S.; Sandro, S.; Gabriele, S.; Ari, P. S.; Alexander, S.; Paolo, U.; Renata, M. W. *Journal of Physics: Condensed Matter* **2009,** 21, (39), 395502.
6. Monkhorst, H. J.; Pack, J. D. *Phys Rev B* **1976,** 13, (12), 5188-5192.
7. Lee, S. W.; McDowell, M. T.; Choi, J. W.; Cui, Y. *Nano Letters* **2011,** 11, (7), 3034-3039.